The Unexpected Role of Fluorine in the Band Gap Narrowing of Silver Niobium and Tantalum Pyrochlore Oxyfluorides

Moussa, Celine; Pourpoint, Frédérique; Saitzek, Sébastien; Famprikis, Theodosios; Roussel, Pascal; Kabbour, Houria; Boivin, Edouard

DOI
10.1021/acs.inorgchem.4c05119

Publication date
2025

Document Version
Final published version

Published in
Inorganic chemistry

Inorganic Chemistry

pubs.acs.org/IC Article

The Unexpected Role of Fluorine in the Band Gap Narrowing of Silver Niobium and Tantalum Pyrochlore Oxyfluorides

Celine Moussa, Frédérique Pourpoint, Sébastien Saitzek, Theodosios Famprikis, Pascal Roussel, Houria Kabbour, and Edouard Boivin*

Cite This: *Inorg. Chem.* 2025, 64, 3898−3907 Read Online

ACCESS | Metrics & More | Article Recommendations | Supporting Information

ABSTRACT: Mixed anion compounds have attracted growing interest in solid-state chemistry as a way to tailor physical properties. In this work, we synthesized new silver niobium and tantalum pyrochlore oxyfluorides by an ion-exchange reaction from $Na_2M_2O_5F_2$ (M = Nb or Ta). Instead of a classical Na^+/Ag^+ cation exchange, a less conventional dual cation and anion exchange reaction ($2\ Na^+ + F^-$)/($Ag^+ + H_2O$) takes place. Indeed, chemical and thermal analyses, as well as Rietveld refinement and ^{19}F NMR, reveal the formation of $AgTa_2O_5F{\cdot}H_2O$ and $Na_{0.4}Ag_{0.8}Nb_2O_5F_{1.2}{\cdot}0.8H_2O$ leading to a significant band gap narrowing of approximately 0.4 eV, as determined by diffuse reflectance spectroscopy. DFT calculations show that Ag 4d−O 2p states are located at the edge of the valence band and that the presence of fluorine in the coordination sphere of Ag promotes the hybridization and hence contributes to the band gap narrowing.

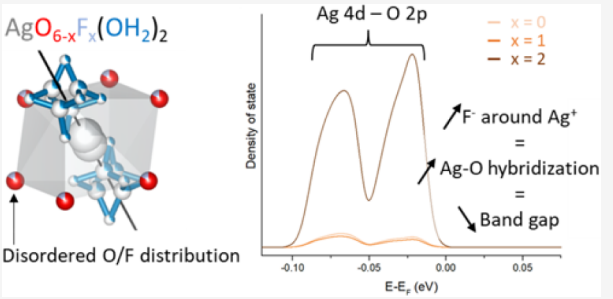

INTRODUCTION

Oxyfluorides offer unique properties that make them suitable for a variety of applications, especially in the field of energy production and storage.[1] Indeed, oxyfluorides appear as promising alternatives to oxides for applications ranging from cathodes[2] and solid-state electrolytes[3] for alkali-ion batteries to anodes of solid oxide[4] or alkaline water electrolyzers.[5] These materials play a pivotal role in advancing energy technologies, as evidenced by the recent emergence of fluoride-ion batteries, where (oxy-)fluorides are integral to all cell components (anode, cathode, and electrolyte).[6] Recently, some pyrochlore oxyfluorides have emerged as efficient and stable OWS photocatalysts, such as $SnTiNbO_6F$ and $Pb_2Ti_2O_{5.4}F_{1.2}$.[7,8] The narrow band gap observed in these materials is essentially due to the ns^2 lone pair (hybridized with (O,F) 2p and M np), located at the edge of the valence band just below the Fermi level. We have recently extended this family of materials through the Na^+/Sn^{2+} ion exchange reaction from $Na_2M_2O_5F_2$, leading to $Na_{2-2x}Sn_xM_2O_5F_2$ (M = Nb^{5+} or Ta^{5+}, $0 < x < 1$) pyrochlore phases.[9] The pyrochlore $A_2B_2X_6X'$ structure is built of a B_2X_6 3D network forming large interconnected hexagonal channels that can be empty (A = □ and X' = □ in FeF_3-type structures,[10] filled with cations (A = Na and X' = □ in $Ag_2Sb_2O_6$-type structures[11] or A = □ and X' = Cs in $RbNiCrF_6$-type structures,[12] with both cations and anions (A = Ca and X' = O in $Ca_2Nb_2O_7$-type structures or A = Ca and X' = O), *etc.*, leading to a wide structural diversity.[13] The great versatility of the A_2X' sublattice has been exploited to tailor the ionic conductivity,[14] ferroelectric,[15] magnetic,[16] multiferroic,[17] photocatalytic,[7,8,18] and optical[19] properties of pyrochlore oxides,[20] oxy-sulfides,[18] oxy-fluorides[21] etc. However, in most pyrochlore oxyfluorides, the oxide anion belongs to the B_2X_6 network, and the fluorine resides only in the A_2X' sublattice. So far, the presence of fluorine in both X and X' sites has been observed in only a few pyrochlore oxyfluorides, such as $SnNb_2O_5F_2$ exhibiting promising photoactivity under sunlight irradiation thanks to a narrow band gap, interestingly narrower than the corresponding oxides due to the crucial role of ionic bonding in the lone pair expression.[9,22,23]

Although Ag^+ does not have this ns^2 electronic configuration, its incorporation into pyrochlore phases tends to strongly reduce the band gap (Eg). This effect is observed, for instance, through the exchange of Ag^+ for K^+ in pyrochlore niobates (from Eg = 3.6 to 2.5 eV)[24] and in O-deficient pyrochlore $Ag_2Sb_2O_6$, which absorbs in the visible region (Eg = 2.7 eV).[25] Similar effects of Ag on the band gap are also observed in other structural types, such as perovskites (Eg = 3.4 eV and 2.8 eV for $NaNbO_3$ and $AgNbO_3$, respectively),[26] and thus silver-based compounds are largely employed for photocatalysis.[27] A general trend in silver-based oxides is that the shorter the Ag−O bond lengths, the narrower the band gap

Received: November 29, 2024
Revised: January 21, 2025
Accepted: February 4, 2025
Published: February 20, 2025

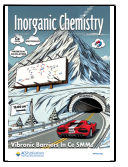

due to Ag 4d-O 2p hybridized orbital raising at the Valence Band Maximum (VBM).[28] Hence, the introduction of fluorine into silver-based oxides may make the Ag−O bond more covalent through an antagonistic effect and could further reduce the band gap. Beyond the photon absorption, electron−hole transport properties are essential for such an application, and polar structures greatly enhance them.[29] In the pyrochlore-type $Ag_2Nb_2O_5F_2$ crystallizing in the polar space group *Ima*2, distortions in the octahedral environments of both Ag^+ and Nb^{5+} sites are observed. Such distortions arise from the propensity toward off-centering of the second-order Jahn−Teller (SOJT) d^0 Nb^{5+} or d^{10} Ag^+ cations, as well as from the heteroleptic coordination associated with O/F anionic mixing.[30] Hence, further exploration of pyrochlore phases containing these elements may lead to new materials that combine strong visible light absorption and efficient charge-carrier separation and transport.

In this article, we report two new pyrochlore oxyfluorides, $AgTa_2O_5F{\cdot}H_2O$ and $Na_{0.4}Ag_{0.8}Nb_2O_5F_{1.2}{\cdot}0.8H_2O$, obtained by a dual cation/anion exchange reaction ($(2\ Na^+ + F^-)/Ag^+ + H_2O$)) from the corresponding $Na_2M_2O_5F_2$ (with M = Nb or Ta). Their crystallographic structure—characterized by Powder X-ray and Neutron Diffraction and Nuclear Magnetic Resonance experiments—and electronic structure—evaluated by Density Functional Theory calculations and Diffuse Reflectance Spectroscopy —are discussed in detail. The substitution of Ag for Na does reduce the band gap (by approximately 0.4 eV) but to a lesser extent than previously reported in other pyrochlore phases.[24] The weakly hybridized Ag 4d-(O/F) 2p states, located near the Fermi level, are responsible for this band gap narrowing. Interestingly, equatorial F^- tends to shorten the apical Ag−O(H_2) bond length, which , in turn, populates these high-energy Ag states.

EXPERIMENTAL SECTION

Approximately 1 g of $Na_2M_2O_5F_2$ (with *M* = Nb or Ta) is synthesized from Nb_2O_5 (Sigma-Aldrich, 99.9%) or Ta_2O_5 (Sigma-Aldrich, 99.9%) in 15 mL of a 2 M NaF (Sigma-Aldrich, >99%) under hydrothermal conditions at 240 °C for 60 h, as previously reported.[31] Heating and cooling rates were set at 1 °C/min. $Na_2M_2O_5F_2$ was used for ion exchange reactions using an $AgNO_3$ solution in water (15 mL, 2 M). Other solvents, such as acetonitrile and diluted ammonia, were used to better understand the reaction mechanism. The reactions were conducted at room temperature for 92 h in the dark. The powder was then filtered, washed several times with water, and rinsed with ethanol prior to being dried at 80 °C in an oven for 1 h. The deuterated samples were obtained by similar ion-exchange reactions using 2 M $AgNO_3$ solutions in D_2O.

X-ray powder diffraction (XRPD) analysis was performed at room temperature in a 2θ range of 10−120° with a scan step width of 0.02° using a Rigaku SmartLab copper rotating anode diffractometer, in Bragg−Brentano geometry, equipped with a 1D D/teX Ultra250 detector.

Neutron powder diffraction (NPD) experiments were performed at the PEARL diffractometer of the Reactor Institute Delft (TU Delft, The Netherlands).[32] Approximately 1 g of deuterated samples were loaded in a 6 mm diameter V−Ni null-scattering-alloy can. The sample can was then placed in a neutron-transparent vacuum box connected to a primary vacuum ($\sim 10^{-3}$ mbar). The diffractogram was measured using a wavelength of 1.667 Å, selected using the (533) reflection of a Ge [511] monochromator. The instrument background, determined from measurements of the empty can, was subtracted from the raw diffractogram.

Analysis of diffraction data was performed via Rietveld refinements against XRPD and NPD using Fullprof.[33] The instrumental resolution functions of the XRPD and NPD instruments were determined empirically from a fundamental parameter set determined by using a reference scan of LaB_6 (NIST 660a) and Al_2O_3 (NIST 676a), respectively.

Fluorine ion-selective ionometry was employed to determine the fluorine mass fraction in the pyrochlore oxyfluorides using an Eu-doped LaF_3 electrode (ORION 9409BN Fluoride Half Cell ISE). Approximately 40 mg of samples were hydrolyzed by 100 mg of KOH in 1 mL of distilled water in a sealed PTFE container at 85 °C overnight. After dilution in 1 L of distilled water, 10 mL is transferred into 10 mL of Total Ionic Strength Adjustment Buffer (TISAB) prior to measuring the potential versus a standard silver chloride electrode (ORION 900100 Sure-Flow Single Junction). The fluorine concentration in the solution was extrapolated from a calibration obtained with NaF standard solutions.

X-ray fluorescence (XRF) spectra were collected using a Bruker S2 Ranger spectrometer equipped with a Pd source and an energy-dispersive SDD detector. The samples were mixed with 50 wt % of cellulose and then pressed into pellets. The spectra were analyzed using Spectra EDX software from Bruker.

Thermogravimetric analysis (TGA) was performed on a TGA-92 thermobalance (Setaram) under an O_2 atmosphere. The evolved gases were monitored by an Omnistar quadrupole mass spectrometer (MS, Pfeiffer) by continuously scanning in the range of 0−100 amu. In order to control the atmosphere, the whole thermobalance was evacuated and filled with the carrier gas before heating the samples up to 950 °C at a rate of 5 °C/min.

Infrared (IR) spectra of the samples were recorded with a PerkinElmer spectrometer, between 4000 and 400 cm^{-1} with 4 cm^{-1} spectral resolution. For each spectrum, 10 scans were averaged by taking air as a reference.

UV−vis diffuse reflectance spectra were collected at room temperature using a PerkinElmer Lambda 650 spectrophotometer in the 200−800 nm range. Before the measurement, the blank was measured using $BaSO_4$ (standard for 100% reflectance) in order to calibrate the device. The reflectance spectra are converted to apparent absorption spectra using the Kubelka−Munk function, $\alpha = (1 - R)^2/2R$. The method of Zanatta,[34] allowing a better estimation of the band gap (Eg) of polycrystalline materials than the Tauc plot, has been used to determine Eg. The indirect band gap is estimated as follows: $Eg = E^{BOLTZ} - 4.3\delta E$, where E^{BOLTZ} is the energy at which the absorption coefficient $\alpha(E^{BOLTZ}) = (\alpha_{min} + \alpha_{max})/2$; α_{min} and α_{max} stand for the minimum and maximum of the absorption coefficient, and δE is used to fit the profile of the $\alpha(E)$ curve near the absorption edge using the following equation:

$$\alpha(E) = \alpha_{max} + \frac{\alpha_{min} - \alpha_{max}}{1 + \exp\left(\frac{E - E^{BOLTZ}}{\delta E}\right)}$$

Transient photocurrent measurements were carried out using a potentiostat/galvanostat (PGSTAT204 -FRA32M, Metrohm). The photoelectrochemical cell (MM-PEC 15 mL single-sided magnetic mount, Redox.me) is made up of the pyrochlore sample coated on an ITO glass (Delta Technologies , LTD) as

https://doi.org/10.1021/acs.inorgchem.4c05119
Inorg. Chem. 2025, 64, 3898−3907

the working electrode, immersed in an electrolyte of an aqueous solution of 0.1 M Na_2SO_4 (pH = 6.6). A platinum electrode and a standard Ag/AgCl electrode were used as the counter and reference electrodes, respectively. To form the working electrode, the crushed powder is added to a mixture of water and N,N-Dimethylformamide (DMF) solvents with a 1:1 ratio. The paste obtained is then deposited on the ITO/glass substrate by the drop casting method and dried at 80 °C for a few minutes in order to obtain a uniform layer. All the measurements were controlled with the Nova2.0 software, allowing regulation of the excitation wavelength of different LEDs with low spectral dispersion (450, 470, 505, 530, 590, 617, 627, and 655 nm) as well as the luminous flux (from 0 to 126 mW/cm^2).

Density Functional Theory (DFT) calculations were carried out by employing the projector augmented wave (PAW)[35,36] method implemented in the Vienna Ab Initio Simulation Package (VASP)[37] and the generalized gradient approximation of Perdew, Burke, and Ernzerhof[38] (PBE) for the exchange-correlation functionals. Owing to the partially disordered character of the O/F distribution of the experimental structure, a particular anionic configuration was selected among the possible configurations. For our DFT models, we have chosen the particular Ag/□ distribution on the A site, which implies that all H_2O molecules are surrounded by two Ag^+ and two vacancies. In the starting model, Ag was located at the 16d position, and it could move away from this position during the structural optimization process. Also, an O/F and Ag/□ distribution on the X and A sites was chosen such that the value of x in the $AgO_{6-x}F_x(H_2O)_2$ polyhedra varies from 0 to 2. Geometry optimizations at fixed unit cell parameters were carried out by using a plane wave energy cutoff of 550 eV and 63 k points in the irreducible Brillouin zone. It converged with residual Hellmann-Feynman forces on the atoms smaller than 0.03 eV/Å. The relaxed structures were used to calculate accurate electronic structure. For the latter, a plane wave cutoff energy of 550 eV and a self-consistent field energy convergence threshold of 10^{-6} eV were used, with 260 k points in the irreducible Brillouin zone. The COHP (Crystal Orbital Hamilton Population) analysis was carried out in the framework of the LOBSTER software.[39−41]

^{19}F Solid-State Nuclear Magnetic Resonance (NMR) experiments were recorded on a Bruker wide bore spectrometer equipped with a 9.4 T magnet corresponding to an ^{19}F Larmor frequency of 376.5 MHz. The spectra were acquired with a 2.5 mm double resonance probe HX spinning at 25 kHz. The ^{1}H channel was tuned to the ^{19}F frequency. One-pulse experiments were used with a radio frequency pulse length of 91 kHz and a recycle delay of 60 s. The number of scans was 200, leading to an experimental time of 3 h 20 min. Spectra were referenced using an external ^{19}F signal of CaF_2 at −108 ppm.

RESULTS AND DISCUSSION

The XRPD patterns of the ion-exchanged samples obtained from $Na_2Ta_2O_5F_2$ and $Na_2Nb_2O_5F_2$ in an aqueous $AgNO_3$ solution are displayed in Figures 1 and S1, respectively. Assuming the ion exchange of Na^+ by Ag^+, the expected reaction is as follows:

$$Na_2M_2O_5F_2 + xAgNO_3 \rightarrow Na_{2-x}Ag_xM_2O_5F_2 + xNaNO_3 \quad (1)$$

XRF has been used to estimate the ratio between the metallic species. The Ag/Nb and Ag/Ta ratio obtained are

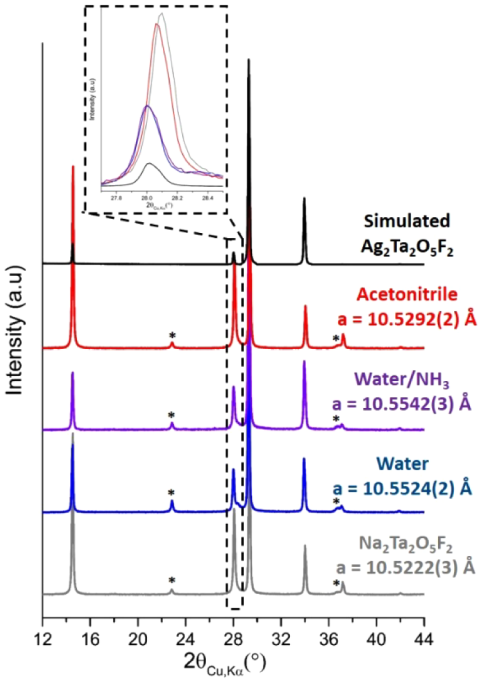

Figure 1. Normalized XRPD patterns of the compounds obtained by ion exchange using an $AgNO_3$ solution in different solvents compared with the starting material ($Na_2Ta_2O_5F_2$) and simulated $Ag_2Ta_2O_5F_2$. * indicates Ta_2O_5 impurity peaks.

0.41 and 0.49 after the ion exchange reaction, while a significantly lower fluorine content is measured by fluorine selective ionometry (3.1 wt % and 5.5 wt % for Nb and Ta phases, respectively; see Table S1) compared to that expected for the product of the **reaction (1)** (i.e., 9.1 wt % for $Ag_{0.82}Na_{1.18}Nb_2O_5F_2$ and 6.2 wt % for $Ag_{0.98}Na_{1.02}Ta_2O_5F_2$). Le Bail refinements reveal that the ion-exchanged phases possess significantly larger cell parameters (a = 10.5534(2) Å for Ta and 10.5494(1) Å for Nb) compared to those observed in the pristine compounds (a= 10.5222(3) Å for Ta and 10.5141(1) Å for Nb). This is in good agreement with the slightly larger radius of Ag^+ compared to Na^+ (r_{Ag+} = 1.28 Å, r_{Na+} = 1.18 Å). This would indicate that an ion-exchange reaction does occur under such conditions, but it may be more complex than a simple Na^+/Ag^+ ion exchange.

As an acidic solution (pH = 2−3) is obtained after dissolving $AgNO_3$ in water, the rather large amount of H_3O^+ in solution may compete with Ag^+ during the ion-exchange reaction. In such a case, the expected reaction is as follows:

$$Na_2M_2O_5F_2 + xAgNO_3 + yH_3O^+ \rightarrow Na_{2-x-y}Ag_x(H_3O)_yM_2O_5F_2 + xNaNO_3 + yNa^+ \quad (2)$$

To try to avoid possible H_3O^+ insertion, the $AgNO_3$ solutions were neutralized (pH = 7−8) with a few drops of diluted ammonia. The XRPD patterns of the products resulting from the ion-exchange reaction in neutralized solutions are also displayed in Figures 1 and S1. Very similar patterns are obtained under these conditions compared to those observed in non-neutralized solutions. This suggests that pH does not play a critical role in this synthesis and that H_3O^+ may not be significantly inserted in the structure, despite the rather acidic pH.

https://doi.org/10.1021/acs.inorgchem.4c05119
Inorg. Chem. 2025, 64, 3898−3907

Another hypothesis is to consider both cation and anion exchange. Indeed, water molecules can be accommodated in the X' site of pyrochlore, as observed, for instance, in $NaW_2O_6.H_2O$ in which the A site is half occupied.[15] To avoid water insertion inside the pyrochlore framework, a dry solvent capable of solubilizing $AgNO_3$, such as acetonitrile, was used. The XRPD patterns of the products resulting from the ion-exchange reaction in acetonitrile are displayed in Figures 1 and S1. XRPD pattern does not show any significant changes, neither in the cell parameters nor in the peak intensity ratio, compared to those observed in the pristine compounds. Therefore, we can assume that no ion-exchange reaction occurs under such conditions.

Thus, we conclude that the substitution of Na^+ by Ag^+ in aqueous media must be accompanied by the substitution of F^- by H_2O, according to the following reaction:

$$Na_2M_2O_5F_2 + xAgNO_3 + xH_2O \rightarrow Na_{2-2x}Ag_xM_2O_5F_{2-x}\cdot x(H_2O) + xNaNO_3 + xNaF \quad (3)$$

To evidence the presence of water in the structure, IR spectroscopy experiments were performed on the initial pyrochlore $Na_2M_2O_5F_2$ and on the ion-exchanged phases (see Figure S2). It reveals a broad band between 3800 and 3400 cm^{-1} with a higher intensity for the ion-exchanged phase. This band, assigned to O−H stretching, is accompanied by another at approximately 1630 cm^{-1} which is typical for H−O−H deformation within a water molecule. Note that the significant O−H contributions observed in the IR spectra of the parent compounds are associated with the partial substitution of Na^+ by H_3O^+, as evidenced previously.[31] The increasing intensity of these bands upon the ion-exchange reaction would indicate an increasing water content within the structure, in good agreement with both reactions 2 and 3.

TGA-MS on the samples obtained in non-neutralized aqueous media under flowing O_2 are shown in Figure S3. In both cases, a loss of mass from 100 to 300 °C, associated with the release of water (m/z = 18), and another from 400 to 950 °C assigned to the loss of HF (m/z ratio of 20) are observed. For the Ta-based compound, the XRPD analysis of the material obtained after the TGA-MS reveals the formation of an $Ag_2Ta_4O_{11}$-type phase in good agreement with the Ag/Ta ratio obtained by XRF. The quantitative analysis of TGA data allows us to exclude the hypothesis of reaction 1) since a significant water loss is observed. According to reactions 2 and 3, knowing the 3.1% of mass loss recorded by the TGA, either $Ag_1(H_3O)_1Ta_2O_5F_2$ (product of reaction 2) or $Ag_1Ta_2O_5F\cdot H_2O$ (product of reaction 3) would be obtained, both in good agreement with XRF. However, the expected weight loss associated with the transformation of $Ag_1(H_3O)_1Ta_2O_5F_2$ to $Ag_2Ta_4O_{11}$ (i.e., 8.1%) is not in agreement with the total weight loss of 5.0% obtained by the TGA. Hence, the hypothesis of **reaction (2)** can be ruled out. Finally, considering now reaction 3 the theoretical weight loss of 5.0 wt % to form $Ag_2Ta_4O_{11}$ closely matches the experiment. Therefore, $Ag_1Ta_2O_5F\cdot H_2O$ seems to be formed, based on XRPD, XRF, TGA-MS, and F^- selective ionometry.

For the ion-exchanged phase obtained in water from $Na_2Nb_2O_5F_2$, the TGA-MAS reveals approximately 3.6 wt % of water mass loss, significantly smaller than the 4.4 wt % expected for dehydration of an $Ag_1Nb_2O_5F_1\cdot H_2O$. Assuming a similar ion exchange mechanism of 2 $Na^+ + F^-$ by $Ag^+ + H_2O$ as for the Ta case, the reaction may be incomplete with the formation of a phase with an approximate composition of $Na_{0.4}Ag_{0.8}Nb_2O_5F_{1.2}\cdot 0.8H_2O$, according to reaction 3. This composition matches well with the weight loss recorded up to 950 °C under O_2 (7.0 wt %, see Figure S3), considering the formation of a mixture between $NaNbO_3$ and $Ag_2Nb_4O_{11}$ (6.9 wt %) observed by the XRPD after TGA.

The compositional study of the compounds suggests the formation of $AgTa_2O_5F\cdot H_2O$ and $Na_{0.4}Ag_{0.8}Nb_2O_5F_{1.2}\cdot 0.8H_2O$ in which the water molecules could be located within the pyrochlore channels, in the X' site, as observed, for instance, in the pyrochlore-like $NaWO_6\cdot H_2O$.[15] In this hypothesis, fluorine should remain at the X site. Therefore, XRPD, NPD, and ^{19}F NMR experiments were performed to evaluate this model.

The Rietveld refinement of the structure of deuterated $AgTa_2O_5F\cdot H_2O$ against both XRPD and NPD data was first performed in the $Fd\bar{3}m$ space group with Ag in a half-occupied 16d position and Ta in the 16c Wyckoff site. The mixed O/F occupancy on the 48f site identified in the parent compounds (i.e., $Na_2Ta_2O_5F_2$) was considered unchanged in the ion-exchanged phases. O_w (i.e., O involved in H_2O molecules) was located on the 32e and H^+ on the 48f site, as observed in $NaWO_6\cdot H_2O$.[15] However, the Fourier map around the 16d position of Ag^+ shows a spreading of the electronic density along the 3-fold axis of the cubic lattice, which is associated with the displacement of Ag^+ away from the inversion center of the A site, as also observed in $Ag_2Nb_2O_5F_2$. This led us to consider the displacement of Ag^+ cations in the 32e Wyckoff position, with an occupancy close to 1/4 (i.e., 0.254 (3)). The result of the refinement is displayed in Figure 2 and summarized in Table 1 which shows excellent agreement between the refined occupancies and the composition determined by XRF, TGA-MS, and F^- selective ionometry.

For the Nb-phase, the refinement against NPD and XRPD data has been performed using a mixed $Na_2Nb_2O_5F_2$−$AgNb_2O_5F\cdot H_2O$ model, constraining the composition to $Na_{2-2x}Ag_xNb_2O_5F_{2-x}(H_2O)_x$ and locating Na on the 16d site

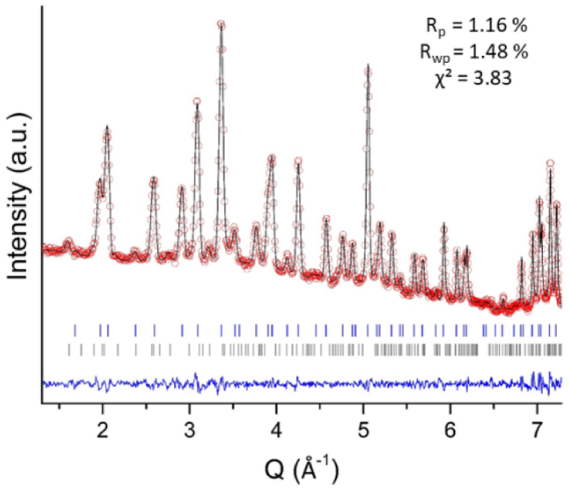

Figure 2. Rietveld refinement of the structure of deuterated $AgTa_2O_5F\cdot H_2O$ against the NPD data. Red dots correspond to the experimental diffraction patterns, the black line is the calculated diffraction patterns, and the blue line is the difference plots. The blue and gray ticks indicate Bragg contributions of $AgTa_2O_5F\cdot H_2O$ and Ta_2O_5 (<2 wt %), respectively. The refinement procedure and refined parameters are summarized in Table 1.

https://doi.org/10.1021/acs.inorgchem.4c05119
Inorg. Chem. 2025, 64, 3898−3907

Table 1. Refined Structural Parameters of Deuterated $AgTa_2O_5F{\cdot}H_2O$ Obtained from Rietveld Refinement of the Structures against NPD Data

$AgTa_2O_5F{\cdot}(D,H)_2O$.							
SG:$Fd\bar{3}m$, Z = 8			a = 10.5422(2)Å				
site[a]	atoms	Wyckoff position	x	y	z	occupancy[b]	U_{iso}
A	Ag	*32e*	0.487(1)	0.487(1)	0.487(1)	0.254(3)	0.019(2)
B	Ta	*16c*	0	0	0	1	0.010(1)
X	O	*48f*	0.3131(3)	1\8	1\8	0.846(9)[c]	0.013(3)[e]
X	F	*48f*	0.3131(3)	1\8	1\8	0.169(2)[c]	0.013(3)[e]
X'	O_w	*32e*	0.4040(2)	0.4040(2)	0.4040(2)	0.250(6)	0.022(3)
	H_w	*48f*	0.5075(4)	1\8	1\8	0.069(6)[d]	0.013(2)[f]
	D_w	*48f*	0.5075(4)	1\8	1\8	0.264(6)[d]	0.013(2)[f]

[a]Site refers to the $A_2B_2X_6X'$ general formula of pyrochlores. [b]Refined composition: $Ag_{1.02(1)}Ta2O_{5.07(5)}F_{1.01(1)}H_{0.41(4)}D_{1.58(4)}O_{w\ 1.00(2)}$. [c]F/O ratio constrained to be equal to 1/5. [d]Constrained to be equal. [e]Sum constrained to be equal to twice the occupancy of O_w. [f]Constrained to be equal.

and F' on the 8b site, as determined previously for $Na_2Nb_2O_5F_2$ (see Figure S4 and Table S2). The refinement of the occupancies leads to an x value of 0.80(1), close to that obtained from XRF, TGA-MS, and F^- selective ionometry.

Nb and Ta are in an octahedral site with Nb−X and Ta−X distances of 1.989(2) and 1.978(2) Å, respectively, leading to BVS in good agreement with pentavalent Nb (BVS = 4.76(6)) and Ta (BVS = 4.98(2)). Ag occupies a site coordinated by 6 O/F anions and 2 H_2O molecules with Ag−O/F ranging between 2.66(2) Å and 2.72(2) Å for Nb-based compounds, and between 2.69(1) Å and 2.76(1) Å for Ta-based ones. However, due to the splitting of both Ag and O_w positions, powder diffraction experiments do not allow for accurately determining the Ag−O_w distances, which depend on the local distribution of the latter around the former and *vice versa*. The refinement of the position of H^+ leads to O_w−H distances (0.97(3) Å for Nb and 1.03(3) Å for Ta) in good agreement with typical O−H bond lengths in water molecules. Moreover, hydrogen bonding is formed across the pyrochlore channel with H--O distances of 2.08(3) Å and 2.05(3) Å for Nb and Ta-based phases, respectively. Overall, 1/3 of the anions located at the 48f position—whether occupied by O or F—are involved in a hydrogen bond.

Owing to the compositional and positional disorder of the structure (i.e., Ag position splitting, Ag/□ mixed occupancy, F and O_w distribution on 32e and 8b as well as disordered O/F distribution on the 48f site), powder diffraction does not allow us to properly describe the impact of the ligand distribution on the metal environments. For this concern, DFT calculations have been conducted using the models described in the experimental section. Note that, although the product of the ion exchange reaction from $Na_2Nb_2O_5F_2$ has a composition significantly different from $AgNb_2O_5F{\cdot}H_2O$, this composition and its Ta analog ($AgTa_2O_5F{\cdot}H_2O$) have been considered for the DFT calculations. The details of the Ag−O/F distances in the relaxed DFT structures of the $AgM_2O_5F{\cdot}H_2O$ models are given in Table S3. Ag has been displaced away from centrosymmetric 16d positions with an average displacement close to that observed by diffraction, leading to an alternation between short ($d(Ag{-}O_w)_{min}$ = 2.36 Å on average) and long ($d(Ag{-}O_w)_{max}$ = 2.52 Å on average) bonds within AgO_w sublattice. BVS of Ag in these relaxed DFT models (0.95 and 0.96 for Nb and Ta-based phases, respectively, on average on 8 Ag^+ cations) are in better agreement with the expected oxidation states than those determined from the average structure obtained by diffraction.

This structural model, depicted in Figure 3, has been evaluated with ^{19}F solid-state NMR. The NMR spectrum of

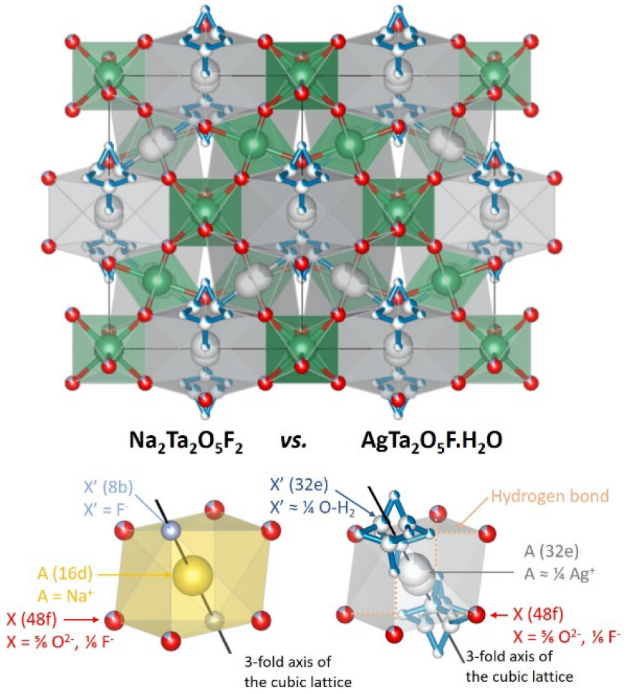

Figure 3. Structure of $AgTa_2O_5F{\cdot}H_2O$ as determined from NPD and comparison of the Ag environment with the one observed for Na in $Na_2Ta_2O_5F_2$.

$AgTa_2O_5F{\cdot}H_2O$ is shown in Figure 4a with the simulation using DMfit software.[42] The fitted data are summarized in Table 2. Two broad (fwhm = 6690 and 3727 Hz, where fwhm denotes the full-width at half-maximum) and intense contributions arising at −76.5 and −98.3 ppm are observed, together with a tiny (0.1% of total integrated intensity) and sharp (fwhm = 339 Hz) signal with a chemical shift of −122.1 ppm. Importantly, the integrated intensity ratio between the two broad contributions is close to 2:1. If the small peak can be assigned to the presence of a tiny amount of F remaining on the X' site associated with a slight Ag overstoichiometry (i.e., composition $Ag_{1+\varepsilon}Ta_2O_5F_{1+\varepsilon}{\cdot}(1-\varepsilon)H_2O$), in good agreement with the Rietveld refinement, the two main ones can be associated with fluorine on the X site, while the splitting may be due to the presence of 1/3 hydrogen-bonded fluorine.

https://doi.org/10.1021/acs.inorgchem.4c05119
Inorg. Chem. 2025, 64, 3898−3907

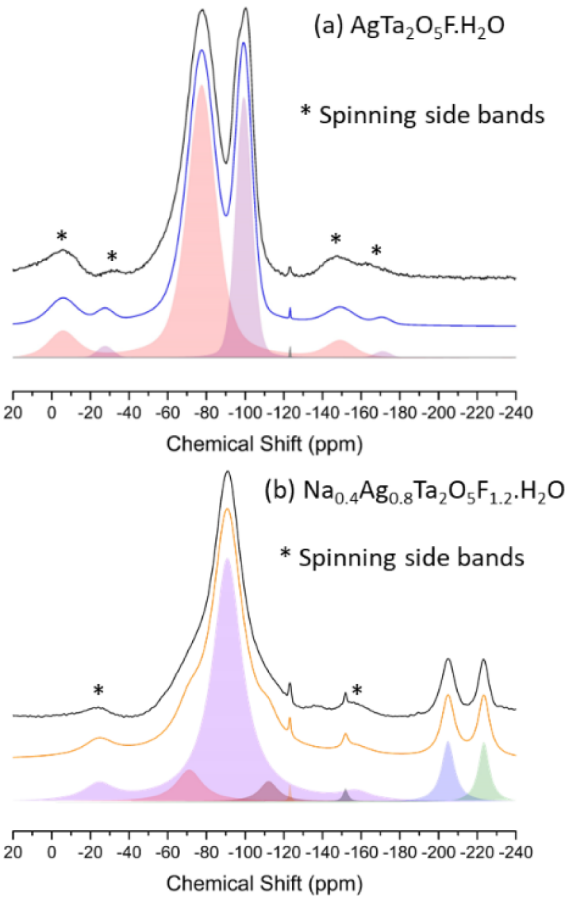

Figure 4. ^{19}F NMR spectra of (a) $AgTa_2O_5F{\cdot}H_2O$ and (b) $Na_{0.4}Ag_{0.8}Nb_2O_5F_{1.2}{\cdot}0.8H_2O$. Black spectra correspond to the experiments, while the yellow and the blue spectra correspond to the fitted spectra.

Table 2. Summary of the Fitted pParameters of the ^{19}F NMR Spectra

shift (ppm)	fwhm (Hz)	intensity (%)	assignment
	$AgTa_2O_5F{\cdot}H_2O$		
−76.5	6690	67.3	F−$Ta_2Ag_1\square_1$
−98.3	3727	32.6	(H--)F−$Ta_2Ag_1\square_1$
−122.1	339	0.1	F'-$Ag_2\square_2$
	$Na_{0.4}Ag_{0.8}Nb_2O_5F_{1.2}{\cdot}0.8H_2O$		
−70.1	6212	7.7	F−$Nb_2Ag_xNa_y$
−89.8	7078	75.2	F−$Nb_2Ag_1\square_1$
−111.2	4367	3.6	F−Nb_2Na_2
−122.1	452	0.3	F'-$Ag_2\square_2$
−150.9	1133	0.6	F'-Ag_1Na_2
−203.9	3069	7.3	F'-$Na_3\square_1$
−222.4	2657	5.3	F'-Na_4

The ^{19}F MAS NMR signature of $Na_{0.4}Ag_{0.8}Nb_2O_5F_{1.2}{\cdot}0.8H_2O$ is more complex (see Figure 4b and Table 2). Seven contributions are observed resonating at −222.5, −203.9, −150.9, −122.1, −111.2, −89.8, and −70.1 ppm. Similar to $Na_2Nb_2O_5F_2$ the first two resonances can be attributed to the residual fluorine residing in the X' site and in a Na-rich environment, while the peak at −222.5 ppm is attributed to F in an X'Na_4 environment, and the one at −203.9 ppm could be attributed to F'$Na_3\square$ defects. The larger intensity of the latter contribution in $Na_{0.4}Ag_{0.8}Nb_2O_5F_{1.2}.0.8H_2O$ compared to that observed in $Na_2Nb_2O_5F_2$ (see Figure S5) could be due to the fact that each inserted Ag^+ generates a vacancy nearby, and the larger concentration of vacancies in the ion-exchange phases induces a higher F'$Na_3\square$/F'Na_4 ratio than observed in $Na_2Nb_2O_5F_2$. If a random $Na^+/Ag^+/\square$ distribution within the channel was adopted, then $FNa_3\square_1$ and FNa_4 should contribute to less than 1% of the total integrated intensity. Hence, the 5.3 and 7.3% observed experimentally would indicate that small clusters with high Na^+ content may be formed within an Ag-rich matrix. Moreover, this distribution would lead to a similar F'Na_4 environment within these $Na_2Nb_2O_5F_2$-type clusters, compared to that observed in the $Na_2Nb_2O_5F_2$ phase, in good agreement with the fact that the corresponding peaks resonate at a very similar frequency in $Na_{0.4}Ag_{0.8}Nb_2O_5F_{1.2}{\cdot}0.8H_2O$ and $Na_2Nb_2O_5F_2$. Moreover, the tiny contribution arising at −150.9 ppm would be associated with the minor fraction of F in the X' site at the edge of these Na-rich clusters, surrounded by Na on one side and Ag on the other side of the frontier (i.e., F'-$Ag_1Na_2\square_1$). Finally, regarding the sharp and small peak at −122.1 ppm, a similar conclusion to the one discussed for $AgTa_2O_5F{\cdot}H_2O$ can be made with F' in an Ag-rich environment (i.e., F'-$Ag_2\square_2$). They indeed resonate at the same frequency because the X' site is not expected to be influenced by the nature of the d^0 metal.

Let us now focus on the fluorine on the X site, whose NMR signature is also different from that of $AgTa_2O_5F{\cdot}H_2O$. First, the contribution at −111.2 ppm is similar to that observed in $Na_2Nb_2O_5F_2$ for F in a Nb_2Na_2 environment (see Figure S5). It would therefore correspond to F located in the X site of Na-rich clusters. The main contribution, located at −89.8 ppm—i.e., in between the two main peaks observed for $AgTa_2O_5F{\cdot}H_2O$—may include both hydrogen-bonded and "free" fluorine which, due to the disorder, arise as a single broad contribution (i.e., F-$Nb_2Ag_1\square_1$). Finally, the resonance at −70.1 ppm could be assigned to F in the X site at the edge of the Na-rich and Ag-rich domains (i.e., F-$Nb_2Ag_xNa_y$). According to these hypotheses, the F'/F ratio in $Na_{0.4}Ag_{0.8}Nb_2O_5F_1F'_{0.2}{\cdot}0.8H_2O$ deduced from ^{19}F NMR (13.5/86.5 = 0.16) matches well with that expected for the estimated composition (i.e., 0.2).

The optical band gap of these new pyrochlore-type oxyfluorides was estimated by UV−visible diffuse reflectance spectrometry (Figure 5). The method reported by Zanatta et al.[34] has been used to determine the band gaps (see Figure S6). Assuming indirect transitions, Eg is 3.70 eV for $AgTa_2O_5F{\cdot}H_2O$ and 3.62 eV for $Na_{0.4}Ag_{0.8}Nb_2O_5F_{1.2}{\cdot}0.8H_2O$. Although a band gap narrowing of approximately ΔEg = 0.4 eV is observed upon $(2\ Na^+ + F^-)/(Ag^+ + H_2O)$ exchange, it is less pronounced than that observed previously in other pyrochlore-type materials.[24] According to the empirical method proposed by Butler and Ginley[43]—which has been demonstrated to yield accurate band edge positions for numerous materials, including the parent compounds[31]—and in spite of the fact that Ag for Na substitution makes both CBM and VBM more oxidative due to the higher electronegativity of the former, both ion-exchanged phases possess suitable band edge alignment for the OWS (see Figure 5) reaction.

In order to understand the band gap narrowing mechanism observed upon the ion-exchange reaction, the electronic structures have been calculated from the relaxed structures described above (Figures 6 and S7). A smaller calculated band gap than the experimentally determined one (3.0 eV for $AgTa_2O_5F{\cdot}H_2O$) is obtained from DFT, in good agreement with the expected underestimation from the GGA method. As

https://doi.org/10.1021/acs.inorgchem.4c05119
Inorg. Chem. 2025, 64, 3898−3907

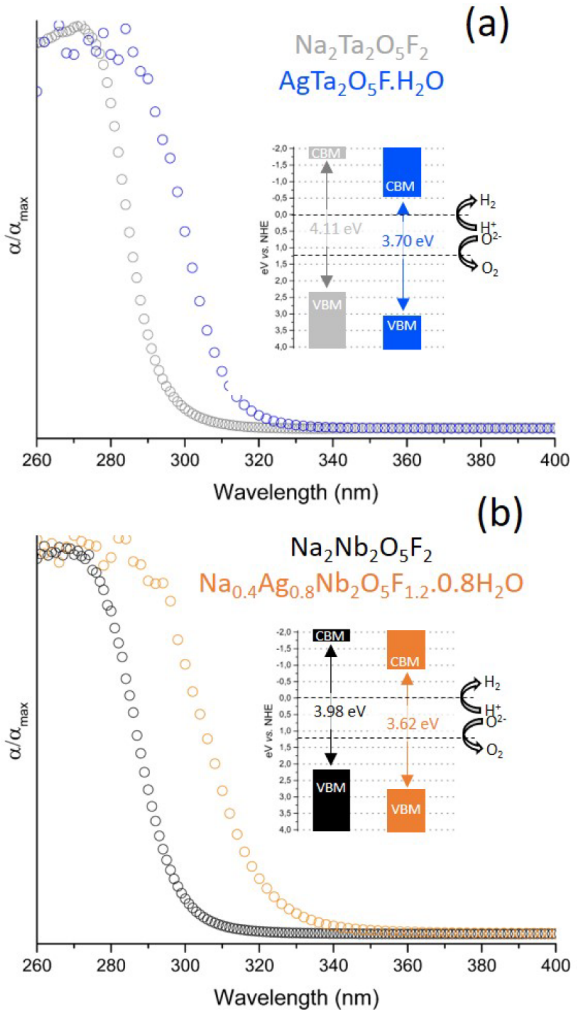

Figure 5. Diffuse reflectance spectra of (a) $AgTa_2O_5F{\cdot}H_2O$ and (b) $Na_{0.4}Ag_{0.8}Nb_2O_5F_{1.2}{\cdot}0.8H_2O$ and their band alignment.

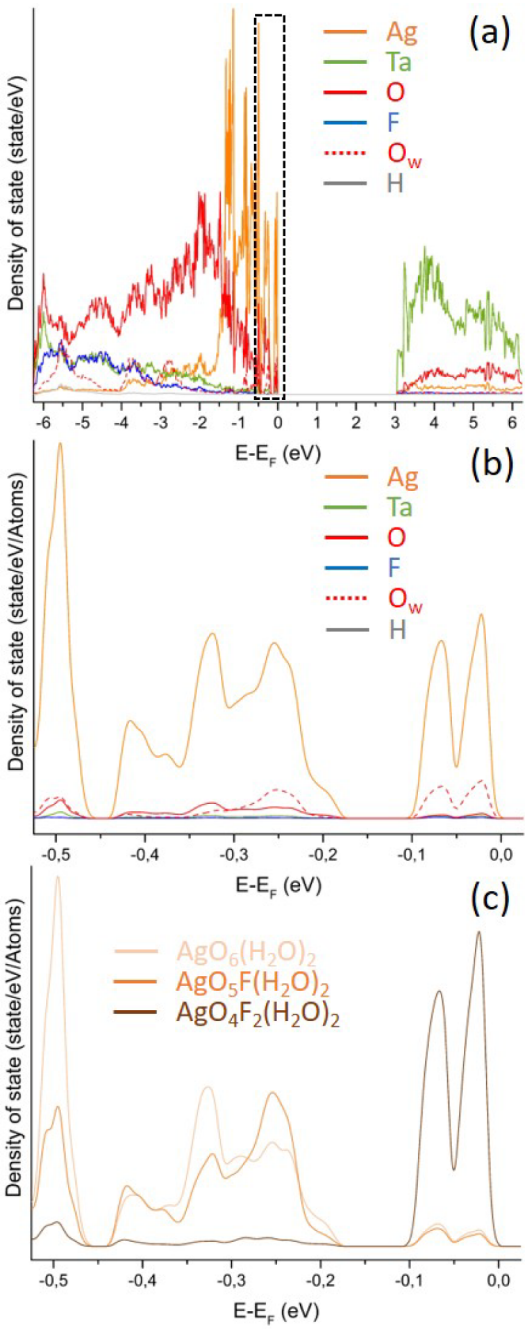

Figure 6. (a) PDOS of $OAgTa_2O_5F{\cdot}H_2O$ with (b) the enlargement of the [−0.525 + 0.025 eV] region mainly composed of Ag 4d−O_w 2p hybridized states (O_w refers to O involved in a H_2O molecule) and (c) the contributions of the Ag in different $AgO_{6-x}F_x(H_2O)_2$ environment showing the fluorine role in the presence of the high-energy states.

previously reported, in the pristine $Na_2Ta_2O_5F_2$ compounds, Ta *5d* states dominate at the bottom of the conduction band and O 2*p* states dominate the top of the valence band.[31] In the Ag-containing phases, the topology of the CB is mostly preserved, but the VB shows additional features associated with the Ag 4d states, mainly located between 0 and −1.5 eV. Moreover, isolated valence states near the Fermi level and separated by approximately 0.1 eV from the rest of the valence band are also observed. Although they experience only a subtle hybridization mainly with the surrounding O_w, the O/F distribution around Ag strongly affects them, as revealed by Figures 6b and S7b showing that fluorine in the equatorial X site promotes the presence of these high-energy states. Figure S8 represents the COHP projected on Ag−O bonds and shows that Ag−O_w within $AgO_4F_2(H_2O)_2$ entities contributes most strongly just below the Fermi level. This can be explained by the fact that the shortest Ag−O_w bond lengths are observed in these $AgO_4F_2(H_2O)_2$ entities (Table S3). Indeed, the integral (ICOHP) values of the Ag-anion bonds are roughly proportional to the bond lengths (Figure S8). This is in good agreement with the observation of short Ag−O bond lengths in some other silver-containing oxides leading to the appearance of occupied Ag 4d states near the Fermi level.[26,28] In oxyfluorides, the high ionicity of the Ag−F bond tends to increase the covalency of the antagonist Ag−O bond. Although counterintuitive at first sight, the highly electronegative fluorine could narrow the band gap compared to the corresponding oxide.

The Figure S9 shows the transient photocurrent response of $AgTa_2O_5F{\cdot}H_2O$ and $Na_{0.4}Ag_{0.8}Nb_2O_5F_{1.2}{\cdot}0.8H_2O$ at different lighting power densities, for a constant wavelength of 450 nm and a bias voltage of 0.8 V vs the Ag/AgCl electrode. They exhibit significantly higher photocurrent densities—about an order of magnitude higher than the corresponding parent compounds. However, the photocurrent response does not

https://doi.org/10.1021/acs.inorgchem.4c05119
Inorg. Chem. 2025, 64, 3898−3907

appear to be stable. Indeed, light exposure generates a current peak that generally decreases with an exponential shape corresponding to a stable equilibrium between the transfer and recombination of charge carriers.[44] In the present case, the rather linear decay and the slightly smaller photocurrent measured at 126 mW·cm^{-1} than at 111 mW·cm^{-1}, indicate an instability of the sample. This significant photocorrosion phenomenon may be due to electrochemical reactions triggered by photoinduction or by the application of the bias potential, as well as to a progressive physical degradation of the working electrode in the electrolyte. In order to highlight a chemical alteration, diffuse reflectance spectra were collected before and after irradiation of the sample at 450 nm for 1 h (see Figure S9). While subtle changes in the band gap values are observed after irradiation, there is a clear decrease in the reflectance at low energy (i.e., lower than the band gap), in good agreement with the darkening of the sample observed by visual inspection. This results in the alteration of the operating lifetime of these materials as photocatalysts.

CONCLUSIONS

In this article, we synthesized two new silver niobium and tantalum pyrochlore oxyfluorides via a dual anion−cation exchange (2 $Na^+ + F^-$)/($Ag^+ + H_2O$) reaction from $Na_2M_2O_5F_2$ (M = Nb or Ta). Chemical and thermal analyses, as well as Rietveld refinement, reveal the formation of $AgTa_2O_5F{\cdot}H_2O$ and $Na_{0.4}Ag_{0.8}Nb_2O_5F_{1.2}{\cdot}0.8H_2O$. ^{19}F NMR suggests the presence of a statistical O^{2-}/F^- distribution on the 48f of the $Fd\bar{3}m$ space group in the former material, and the formation of an inhomogeneous $Na^+/Ag^+/\square$ distribution in the latter, where Na-rich clusters reside within an Ag-rich matrix. The exchange of Na by Ag leads to a significant band gap reduction of about 0.4 eV due to Ag 4d−O 2p states localized at the edge of the valence band, as determined by DFT. Moreover, DFT also shows that fluorine in the Ag coordination sphere promotes Ag−O covalency, which unexpectedly leads to a narrower band gap. These findings not only provide new insights into the structural and electronic effects of fluorine in new silver-based pyrochlore oxyfluorides but also suggest strategies to design advanced materials with controlled band structures that may find applications in numerous fields.

ASSOCIATED CONTENT

Supporting Information

The Supporting Information is available free of charge at https://pubs.acs.org/doi/10.1021/acs.inorgchem.4c05119.

XRPD patterns of the compounds obtained by ion exchange using an $AgNO_3$ solutions from $Na_2Nb_2O_5F_2$; Ag/M ratio obtained by XRF, weight fraction of fluorine obtained by F^- selective ionometry and weight loss obtained by TGA for $AgTa_2O_5F{\cdot}H_2O$ and $Na_{0.4}Ag_{0.8}Nb_2O_5F_{1.2}{\cdot}0.8H_2O$; IR spectra of the parent $Na_2M_2O_5F_2$ and the corresponding ion-exchanged phases; TGA-MS of $AgTa_2O_5F{\cdot}H_2O$ and $Na_{0.4}Ag_{0.8}Nb_2O_5F_{1.2}{\cdot}0.8H_2O$ under O_2; Joint Rietveld refinement of the structure of $Na_{0.4}Ag_{0.8}Nb_2O_5F_{1.2}{\cdot}0.8H_2O$ against both XRPD and NPD data and refined structural parameters;^{19}F NMR spectra of $Na_2Nb_2O_5F_2$; fit of the α(E) curves using the function of Zanatta; PDOS of $AgNb_2O_5F{\cdot}H_2O$; Ag−O/F distances of the relaxed DFT structures of $AgTa_2O_5F{\cdot}H_2O$ and $AgNb_2O_5F{\cdot}H_2O$; COHPs analysis for $AgTa_2O_5F{\cdot}H_2O$; The Photocurrent density as a function of time at different incident flux (Φ) and with V_{bias} = 0.8 V vs Ag/AgCl and λ = 450 nm for $AgTa_2O_5F{\cdot}H_2O$ and $Na_{0.4}Ag_{0.8}Nb_2O_5F_{1.2}{\cdot}0.8H_2O$; Diffuse reflectance of $AgTa_2O_5F{\cdot}H_2O$ and $Na_{0.4}Ag_{0.8}Nb_2O_5F_{1.2}{\cdot}0.8H_2O$ before and after irradiation at 450 nm for 1 h (PDF)

Accession Codes

Deposition Numbers 2404626−2404627 contain the supplementary crystallographic data for this paper. These data can be obtained free of charge via the joint Cambridge Crystallographic Data Center (CCDC) and Fachinformationszentrum Karlsruhe Access Structures service.

AUTHOR INFORMATION

Corresponding Author

Edouard Boivin − *Univ. Lille, CNRS, Centrale Lille, ENSCL, Univ. Artois, Lille F-59000, France; Institut des Molécules et Matériaux Du Mans (IMMM), UMR 6283 CNRS, Le Mans Université, Le Mans 72085, France;* orcid.org/0000-0002-5468-3594; Email: edouard.boivin@univ-lemans.fr

Authors

Celine Moussa − *Univ. Lille, CNRS, Centrale Lille, ENSCL, Univ. Artois, Lille F-59000, France*

Frédérique Pourpoint − *Univ. Lille, CNRS, Centrale Lille, ENSCL, Univ. Artois, Lille F-59000, France; Institut Universitaire de France, Paris F-75005, France*

Sébastien Saitzek − *Univ. Lille, CNRS, Centrale Lille, ENSCL, Univ. Artois, Lille F-59000, France;* orcid.org/0000-0003-1403-5397

Theodosios Famprikis − *Faculty of Applied Sciences, Delft University of Technology, Delft 2629 JB, The Netherlands;* orcid.org/0000-0002-7946-1445

Pascal Roussel − *Univ. Lille, CNRS, Centrale Lille, ENSCL, Univ. Artois, Lille F-59000, France;* orcid.org/0000-0001-7243-7293

Houria Kabbour − *Univ. Lille, CNRS, Centrale Lille, ENSCL, Univ. Artois, Lille F-59000, France; Nantes Université, CNRS, Institut des Matériaux de Nantes Jean Rouxel − UMR6502, Nantes F-44000, France*

Complete contact information is available at: https://pubs.acs.org/10.1021/acs.inorgchem.4c05119

Notes

The authors declare no competing financial interest.

ACKNOWLEDGMENTS

This work was supported by the I-Site (ANR-16-IDEX-0004 ULNE) and by the Région Hauts-de-France (STaRS, accueil de jeunes chercheurs d'avenir). Chevreul Institute (FR CNRS 2638), Ministère de l'Enseignement Supérieur et de la Recherche, Région Nord − Pas de Calais, and FEDER are acknowledged for supporting and funding X-ray facilities. Frédéric Capet (X-ray platform) is also warmly thanked for his help during data collection. The DIM 1 "Energetic efficiency" of the UArtois is thanked for its financial support for photoelectrochemical measurements. T. F. acknowledges the funding provided by the European Union's HORIZON EUROPE program in the form of a Marie Skłodowska-Curie individual postdoctoral fellowship (project no. 101066486).

REFERENCES

(1) Kageyama, H.; Hayashi, K.; Maeda, K.; Attfield, J. P.; Hiroi, Z.; Rondinelli, J. M.; Poeppelmeier, K. R. Expanding frontiers in materials chemistry and physics with multiple anions. *Nat. Commun.* **2018**, *9* (1), 772.

(2) Boivin, E.; David, R.; Chotard, J.-N.; Bamine, T.; Iadecola, A.; Bourgeois, L.; Suard, E.; Fauth, F.; Carlier, D.; Masquelier, C.; et al. $LiVPO_4F_{1-y}O_y$ Tavorite-type compositions: Influence of the vanadyl-type defects' concentration on the structure and electrochemical performance. *Chem. Mater.* **2018**, *30*, 5862−5693.

(3) Aimi, A.; Onodera, H.; Shimonishi, Y.; Fujimoto, K.; Yoshida, S. High Li-Ion Conductivity in Pyrochlore-Type Solid Electrolyte $Li_{2-x}La_{(1+x)/3}M_2O_6F$ (M = Nb, Ta). *Chem. Mater.* **2024**, *36*, 3717−3725.

(4) Shen, Z.; Bassat, J.-M.; Fourcade, S.; Demourgues, A.; Durand, E.; Teule-Gay, L.; Duttine, M.; Gamon, J. Is Fluorine Incorporation in the $La_{0.6}Sr_{0.4}Co_{0.2}Fe_{0.8}O_{3-\delta}$ Improving Its Electrochemical Behavior for Solid Oxide Cells Applications? *Adv. Energy Mater.* **2024**, *14* (32), 2401518.

(5) Terry, A.; et al. Simple and Scalable Synthetic Route for Tunable Compositions of Multimetallic Oxyfluorides as Oxygen Evolution Reaction Catalysts. *ACS Appl. Energy Mater.* **2024**, *7*, 11466.

(6) Nowroozi, M. A.; et al. Fluoride ion batteries - past, present, and future. *J. Mater. Chem. A* **2021**, *9*, 5980−6012.

(7) Kuriki, R.; et al. A Stable, Narrow-Gap Oxyfluoride Photocatalyst for Visible-Light Hydrogen Evolution and Carbon Dioxide Reduction. *J. Am. Chem. Soc.* **2018**, *140*, 6648−6655.

(8) Luo, Y.; Zhou, X.; Zhang, J.; Qi, Y.; Li, Z.; Zhang, F.; Li, C. Development of Sn^{2+}-based oxyfluoride photocatalyst with visible light response of ca. 650 nm via strengthened hybridization of Sn 5s and O 2p orbitals. *J. Energy Chem.* **2021**, *63*, 385−390.

(9) Boivin, E.; et al. New Pyrochlore-like Oxyfluorides Na2−2xSnxM2O5F2 (M = Nb5+ or Ta5+ and $1 < x < 0$) as Potential Candidates for Overall Water Splitting Photocatalysis. *Chem. Mater.* **2023**, *35*, 447−456.

(10) De Pape, R.; Ferey, G. A. new form of FeF3 with the pyrochlore structure: Soft chemistry synthesis, crystal structure, thermal transitions and structural correlations with the other forms of FeF3. *Mater. Res. Bull.* **1986**, *21*, 971−978.

(11) Laurita, G.; Page, K.; Sleight, A. W.; Subramanian, M. A. Structural investigation of the substituted pyrochlore $AgSbO_3$ through total scattering techniques. *Inorg. Chem.* **2013**, *52*, 11530−11537.

(12) Babel, D.; Pausewang, G.; Viebahn, W. Notizen: Die Struktur einiger Fluoride, Oxide und Oxidfluoride AMe 2 X 6: Der RbNiCrF 6 -Typ. *Zeitschrift für Naturforsch. B* **1967**, *22* (11), 1219−1220.

(13) Talanov, M. V.; Talanov, V. M. Structural Diversity of Ordered Pyrochlores. *Chem. Mater.* **2021**, *33*, 2706−2725.

(14) Phraewphiphat, T.; Iqbal, M.; Suzuki, K.; Hirayama, M.; Kanno, R. Synthesis and lithium-ion conductivity of $LiSrB_2O_6F$ (B = Nb^{5+}, Ta^{5+}) with a pyrochlore structure. *J. Japan Soc. Powder Powder Metall.* **2018**, *65*, 26−33.

(15) Saitzek, S.; et al. Ferroelectricity in $La_2Zr_2O_7$ thin films with a frustrated pyrochlore-type structure. *J. Mater. Chem. C* **2014**, *2*, 4037−4043.

(16) Lynn, J. W.; Vasiliu-Doloc, L.; Subramanian, M. A. Spin Dynamics of the Magnetoresistive Pyrochlore $Tl_2Mn_2O_7$. *Phys. Rev. Lett.* **1998**, *80*, 4582−4585.

(17) Dong, X. W.; Wang, K. F.; Luo, S. J.; Wan, J. G.; Liu, J.−M. Coexistence of magnetic and ferroelectric behaviors of pyrochlore $Ho_2Ti_2O_7$. *J. Appl. Phys.* **2009**, *106* (10), 104101.

(18) Ogawa, M.; Suzuki, H.; Tomita, O.; Nakada, A.; Abe, R. Sn^{2+}-based pyrochlore oxysulfides with narrow band gaps for photocatalytic water splitting. *J. Photochem. Photobiol. A Chem.* **2023**, *444*, 114895.

(19) Giampaoli, G.; Li, J.; Hermann, R. P.; Stalick, J. K.; Subramanian, M. A. Tuning color through sulfur and fluorine substitutions in the defect tin(II, IV) niobate pyrochlores. *Solid State Sci.* **2018**, *81*, 32−42.

(20) Laurita, G.; et al. From $Ag_2Sb_2O_6$ to $Cd_2Sb_2O_7$: Investigations on an anion-deficient to ideal pyrochlore solid solution. *J. Solid State Chem.* **2014**, *210*, 65−73.

(21) Galven, C.; et al. New Oxyfluoride Pyrochlores $Li_{2-x}La_{(1+x)/3}\square_{(2x-1)/3}B_2O_6F$ (B = Nb, Ta): Average and Local Structure Characterization by XRD, TEM and ^{19}F Solid-State NMR Spectroscopy. *Eur. J. Inorg. Chem.* **2010**, *2010*, 5272−5283.

(22) Walsh, A.; Payne, D. J.; Egdell, R. G.; Watson, G. W. Stereochemistry of post-transition metal oxides: Revision of the classical lone pair model. *Chem. Soc. Rev.* **2011**, *40*, 4455−4463.

(23) Walsh, A.; Watson, G. W. Influence of the anion on lone pair formation in Sn(II) monochalcogenides: A DFT study. *J. Phys. Chem. B* **2005**, *109*, 18868−18875.

(24) Withanage, I.; et al. Synthesis and crystal structure of pyrochlore-type silver niobate and tantalate. *J. Ceram. Soc. Jpn.* **2017**, *125*, 776−778.

(25) Mizoguchi, H.; Eng, H. W.; Woodward, P. M. Probing the Electronic Structures of Ternary Perovskite and Pyrochlore Oxides Containing Sn^{4+} or Sb^{5+}. *Inorg. Chem.* **2004**, *43*, 1667−1680.

(26) Kato, H.; Kobayashi, H.; Kudo, A. Role of Ag^+ in the band structures and photocatalytic properties of $AgMO_3$ (M: Ta and Nb) with the perovskite structure. *J. Phys. Chem. B* **2002**, *106*, 12441−12447.

(27) Huang, K.; Li, C.; Zheng, Y.; Wang, L.; Wang, W.; Meng, X. Recent advances on silver-based photocatalysis: Photocorrosion inhibition, visible-light responsivity enhancement, and charges separation acceleration. *Sep. Purif. Technol.* **2022**, *283*, 120194.

(28) Hong, H. Y. P.; Kafalas, J. A.; Goodenough, J. B. Crystal chemistry in the system $MSbO_3$. *J. Solid State Chem.* **1974**, *9*, 345−351.

(29) Li, L.; Salvador, P. A.; Rohrer, G. S. Photocatalysts with internal electric fields. *Nanoscale* **2014**, *6*, 24−42.

(30) Vlasse, M.; Chaminade, J.-P.; Saux, M.; Pouchard, M. La structure cristalline de l'oxyfluorure d'argent et de niobium $Ag_2Nb_2O_5F_2$. *Rev. Chim. Miner.* **1977**, *14*, pp. 429−434.

(31) Boivin, E.; et al. An unusual O^{2-}/F^- distribution in the new pyrochlore oxyfluorides: $Na_2B_2O_5F_2$ (B = Nb, Ta). *Chem. Commun.* **2022**, *58*, 2391−2394.

(32) Van Eijck, L.; et al. Design and performance of a novel neutron powder diffractometer: PEARL at TU Delft. *J. Appl. Crystallogr.* **2016**, *49*, 1398−1401.

(33) Rodriguez-Carvajal, J. recent advances in magnetic structure determination by neutron powder diffraction. *Phys. B* **1993**, *192*, 55−69.

(34) Zanatta, A. R. Revisiting the optical bandgap of semiconductors and the proposal of a unified methodology to its determination. *Sci. Rep.* **2019**, *9* (1), 11225.

(35) Bloch, P. E. Projector augmented-wave method. *Phys. Rev. B* **1994**, *50*, 17954−17979.

(36) Kresse, G.; Joubert, D. From ultrasoft pseudopotentials to the projector augmented-wave method. *Phys. Rev. B* **1999**, *59*, 1758−1775.

(37) Kresse, G.; Furthmüller, J. Efficiency of ab-initio total energy calculations for metals and semiconductors using a plane-wave basis set. *Comput. Mater. Sci.* **1996**, *6*, 15−50.

(38) Perdew, J. P.; Burke, K.; Ernzerhof, M. Generalized Gradient Approximation Made Simple. *Phys. Rev. Lett.* **1996**, *77*, 3865−3868.

(39) Deringer, V. L.; Tchougréeff, A. L.; Dronskowski, R. Crystal orbital Hamilton population (COHP) analysis as projected from plane-wave basis sets. *J. Phys. Chem. A* **2011**, *115*, 5461−5466.

(40) Maintz, S.; Deringer, V. L.; Tchougréeff, A. L.; Dronskowski, R. LOBSTER: A tool to extract chemical bonding from plane-wave based DFT. *J. Comput. Chem.* **2016**, *37*, 1030−1035.

(41) Dronskowski, R.; Blöchl, P. E. Crystal orbital Hamilton populations (COHP): energy-resolved visualization of chemical bonding in solids based on density-functional calculations. *J. Phys. Chem.* **1993**, *97*, 8617−8624.

(42) Massiot, D.; et al. Modelling one- and two-dimensional solid-state NMR spectra. *Magn. Reson. Chem.* **2002**, *40*, 70−76.

https://doi.org/10.1021/acs.inorgchem.4c05119
Inorg. Chem. 2025, 64, 3898−3907

(43) Butler, M. A.; Ginley, S. D. Prediction of Flatband Potentials at Semiconductor-Electrolyte Interfaces from Atomic Electronegativities. *J. Electrochem. Soc.* **1978**, *125*, 228−232.
(44) Lewerenz, H.-J.; Peter, L. *Photoelectrochemical Water Splitting: Materials, Processes and Architectures*; Royal Society of Chemistry, 2013.

https://doi.org/10.1021/acs.inorgchem.4c05119
Inorg. Chem. 2025, 64, 3898−3907